Article

A Novel Index for Daily Flood Inundation Retrieval from CYGNSS Measurements

Ting Yang [1,2], Zhigang Sun [1,2,3,4,*] and Lulu Jiang [5]

1   CAS Engineering Laboratory for Yellow River Delta Modern Agriculture, Institute of Geographic Sciences and Natural Resources Research, Chinese Academy of Sciences, Beijing 100101, China
2   Shandong Dongying Institute of Geographic Sciences, Dongying 257000, China
3   Key Laboratory of Ecosystem Network Observation and Modeling, Institute of Geographic Sciences and Natural Resources Research, Chinese Academy of Sciences, Beijing 100101, China
4   College of Resources and Environment, University of Chinese Academy of Sciences, Beijing 100049, China
5   Guangdong Province Key Laboratory for Climate Change and Natural Disaster Studies, School of Atmospheric Sciences, Sun Yat-sen University, Guangzhou 510275, China
*   Correspondence: sun.zhigang@igsnrr.ac.cn; Tel.: +86-10-64889523

Abstract: Since flood inundation hampers human life and the economy, flood inundation retrieval with high temporal resolution and accuracy is essential for the projection of the environmental impact. In this study, a novel cyclone global navigation satellite system (CYGNSS)-based index, named the annual threshold flood inundation index (ATFII) for flood inundation retrieval, is proposed, and the grades of flood inundation are quantified. First, the CYGNSS surface reflectivity with land surface properties (i.e., vegetation and surface roughness) calibration is derived based on the zeroth-order radiative transfer model. Then, an index named ATFII is proposed to achieve inundation retrieval, and the inundation grades are classified. The results are validated with the Visible Infrared Imaging Radiometer Suite (VIIRS) flood product and GPM precipitation data. The validation results between ATFII and GPM precipitation indicate that the ATFII enables flood inundation retrieval at rapid timescales and quantifies the inundation variation grades. Likewise, for monthly results, the R value between the VIIRS flood product and ATFII varies from 0.51 to 0.64, with an acceptable significance level ($p < 0.05$). The study makes contributions in two aspects: (1) it provides an index-based method for mapping daily flood inundation on a large scale, with the advantages of fast speed and convenience, and (2) it provides a new way to derive inundation grade variations, which can help in studying the behavior of inundation in response to environmental impacts directly.

Keywords: CYGNSS; flood inundation; ATFII; VIIRS; index

1. Introduction

Floods are one of the most destructive and unpreventable natural disasters in the world. They are characterized by a high frequency, width, and suddenness. The occurrence of floods has a severe impact on human life and the economy. Flood impact assessment is a multidisciplinary subject of high importance, related to meteorological, hydrological, hydraulic, and environmental sciences and related technologies. In recent years, the ecosystem has undergone large changes due to the frequent occurrence of flood inundation [1–3]. Additionally, a nonmonotonic relationship exists between climate change and flood extremes, and externally forced climate change has been proven to be a causal driver of river flow [4,5]. Thus, the timely and accurate retrieval of flood inundation and quantification of its extent over time can provide a scientific basis for the projection of the climate impact.

Remote sensing, especially spaceborne remote sensing, can provide timely and cost-effective data compared to field observation. Remote sensing collects flood events in a long time series, and also indicates the flood inundation area and informs flood event spatial

variability over a large scale. In addition, remote sensing data can provide a supportive reference for reproducing extreme flood events [6–9]. Common remote sensing approaches to map flood inundation states mainly rely on optical and microwave sensors [10–13]. Optical remote sensing data (e.g., Moderate Resolution Imaging Spectroradiometer (MODIS) and Landsat) have a high spatial resolution (tens or hundreds of meters). Still, they are impacted greatly by clouds and mists, preventing their use in observing flooding events in a timely manner. On the contrary, active microwave sensors, such as synthetic-aperture radar (SAR) missions, generate high spatial resolution (~100 m) but low temporal resolution (~7–14 days), limited in their ability to monitor flooding events with the required spatiotemporal resolution. Passive microwave sensors provide all-sky capability, but gaps exist in daily products and with coarse spatial distributions (tens of kilometers). This also prevents observing flooding event process information in detail [14].

Global navigation satellite system reflectometry (GNSS-R) is a technique that receives the reflected signals from the surface of the Earth. The GNSS-R acts as a bistatic radar and operates at L band microwave signals [15,16]. The cyclone global navigation satellite system (CYGNSS) mission, which is the first spaceborne GNSS-R mission with a constellation of low Earth orbit receivers, was launched into space in December 2016 by NASA. The CYGNSS contains eight microsatellites with a Global Positioning System (GPS)-R payload, which can offer high spatial resolution with low revisit times in measuring global ocean/land geophysical parameters [17]. Compared with passive microwave satellites (i.e., Soil Moisture Active Passive (SMAP) and Soil Moisture and Ocean Salinity (SMOS)), the CYGNSS can provide more frequent sampling with revisiting times of approximately 2.8–7 h per day. The spatial resolution of the CYGNSS can be defined by the first Fresnel zone along the orbit, which was ~6 × 0.5 km until July 2019 and ~3 × 0.5 km after July 2019, depending on whether the signal integration time was 1 s or 0.5 s, respectively [15,18].

The CYGNSS was designed to measure ocean winds in the tropics. Oceanography-related CYGNSS studies mainly concentrate on characterizing wind speed, sea ice, ocean altimetry, and sea surface salinity [19–23]. At present, signals from the CYGNSS are also proved sensitive to land surface properties, such as soil moisture, soil freeze/thaw, flood inundation, wetland extent, and waterbody [2,15,24–30]. Research on flood inundation mapping from CYGNSS data has recently been a popular topic. Chew et al. (2018) made the first attempt to map flood inundation during the 2017 Atlantic hurricane season using CYGNSS data [2]. In 2020, they proposed a forward model describing how the CYGNSS surface reflectivity (SR) changes due to flooding for different land surface types [27]. Wan et al. (2019) proposed a threshold method to monitor flood inundation during typhoons and extreme precipitation events using CYGNSS data [26]. Zhang et al. (2021) used the different sensitivities of the CYGNSS SR on different ground features to obtain the range of flooding in Henan Province, China, during one extreme precipitation event [29]. These results can investigate the feasibility of using CYGNSS signals to obtain flood inundation information, but they are difficult to apply to the realized systematic quantification of inundation and in analyzing its variation characteristics.

This study aims to realize daily flood inundation dynamic retrieval with CYGNSS measurements at rapid timescales. Unlike the aforementioned studies in the context of the CYGNSS, this study proposes an index named the annual threshold flood inundation index (ATFII) to detect the flood inundation state and quantify inundation variations from multiple inundated grades. The index model is constructed according to the relationship between the CYGNSS SR and annual inundation states at the spatial and temporal scales, and the index is applied to characterize the inundation grades. The results are compared with Visible Infrared Imaging Radiometer Suite (VIIRS) flood data and Global Precipitation Measurement (GPM) precipitation data. The influence of land types, the feasibility of using the CYGNSS to detect sub-daily flood inundation processes, and the advantages and limitations of this index are also discussed.

2. Data

2.1. CYGNSS

The application area of the CYGNSS is quasi-global, i.e., from 38°N to 38°S. The CYGNSS mission is a constellation of eight LEO observatories and receives the direct GPS L1-C/A signal and the Earth's surface scattering signals using the Delay Doppler Mapping (DDM) instrument. The Earth's surface scattering signals are then filtered through a time delay and Doppler shift to form a DDM. In other words, the DDM is a diffuse surface scattering map near the specular point (SP). The CYGNSS Level 0 data product is then generated using a coherent integration interval of 1 ms and an incoherent average of 1000 ms [16,31]. Level 1 calibration then converts the raw DDMs of Level 0 into DDMs of received power in watts. This work focuses on the CYGNSS Level 1 version 3.0 product, which can be downloaded via https://podaac.jpl.nasa.gov/, accessed on 1 September 2022.

Two years (January 2020–December 2021) of CYGNSS data are used in this study. The data in 2020 and 2021 were used for estimation and validation, respectively. The CYGNSS data were filtered with an antenna gain greater than 0 dB and quality flags. The quality flags included multi variables, such as "S band transmitter powered up", "spacecraft attitude error", "blackbody DDM", and "low confidence in the GPS EIRP". These steps are frequently used criteria in current CYGNSS research to filter out low quality data in land-related studies [15,32]. The CYGNSS data were then gridded to a 9 km Equal-Area Scalable Earth (EASE) Grid 2.0 cell.

2.2. VIIRS

The Visible Infrared Imaging Radiometer Suite (VIIRS) sensor is onboard the Suomi National Polar-orbiting Partnership (S-NPP) satellite, and it succeeds the MODIS for flood mapping. Compared to the MODIS, the VIIRS has a better spatial resolution (500 m vs. 375 m). The VIIRS operates in shortwave IR bands. The swath width of VIIRS imagery is 300 km, which can provide more spatially complete and daily continuous flood mapping data. The VIIRS daily composited floodwater product with a spatial resolution of 375 m is a near real-time product derived from daytime VIIRS imagery. The floodwater fractions in the VIIRS flood maps indicate the open water areas in each pixel. Moreover, the flood maps generated by the VIIRS flood mapping system are widely used, i.e., FEMA in the USA [33]. In this study, VIIRS floodwater fraction data was used as the reference, to compare with the retrieval inundation results.

2.3. SMAP

The SMAP mission provides global variables (e.g., soil moisture, brightness (TB), temperature, and freeze/thaw) on 3, 9, and 36 km EASE grids. It incorporates a radar and radiometer, both operating at the L band at the incidence angle of approximately 40°. The revisit time of SMAP is 2–3 days [3,15,23]. To calibrate the effects of land surface properties (i.e., vegetation and surface roughness), we used the 2020–2021 Level 3 SMAP TB 9 km gridded data from the radiometer as auxiliary data. In addition, SMAP SM data were used to verify the final results.

2.4. GPM

In addition, to evaluate the temporal dynamics of CYGNSS-derived inundation, daily precipitation data obtained from NASA's GPM IMERG were used. Specifically, precipitation data from the late version (version 6) were used. This dataset was derived from the half-hourly GPM_3IMERGHH, and the derived result represents a late estimate of the daily accumulated precipitation. The GPM precipitation data had a spatial resolution of $0.1° \times 0.1°$ [34]. Simple averaging was used to resample GPM precipitation observations to a 9 km grid to match up with the CYGNSS data.

3. Methods

The technical processing diagram of this study is shown in Figure 1. The method mainly consists of two parts. The first step is to obtain CYGNSS SR with land surface physical property (i.e., vegetation and surface roughness) calibration, hereafter named SR$_{cali}$, based on the approach described by [25]. The next step is to build the ATFII index retrieval model based on the relationship between the time series of the CYGNSS SR$_{cali}$ and annual reference inundation states. Moreover, the inundation grades are classified according to the combined results of the ATFII and VIIRS flood data. The retrieval inundation results are analyzed in temporal dynamics and spatial distributions.
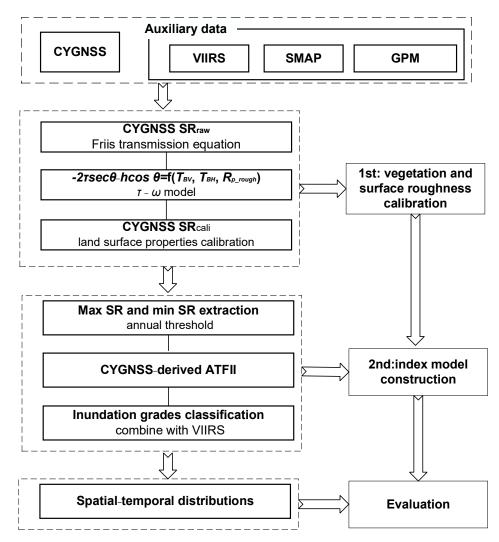

Figure 1. Flowchart of the proposed index in this study to retrieve inundation.

3.1. SR Estimation with Vegetation and Surface Roughness Effect Calibrations

CYGNSS measurement is highly sensitive to water due to its high electric permittivity. However, the footprint of the CYGNSS is always a mixture of multiple elements, such as water, soil, and vegetation. The land surface properties (i.e., vegetation and surface roughness) would reduce the sensitivity of the L band to surface water. Figure 2 shows the absolute error simulations with varying vegetation optical depths (VODs) and surface roughness represented by h parameters. The maximum value of VOD is set to 1, considering the effectiveness of the L band in sensing vegetation, and the maximum value of the h parameter (surface roughness) is set to 1.6. The absolute value of the error varies from 0 to 21.60 dB. It keeps increasing with increases in the VOD and h parameter. Therefore,

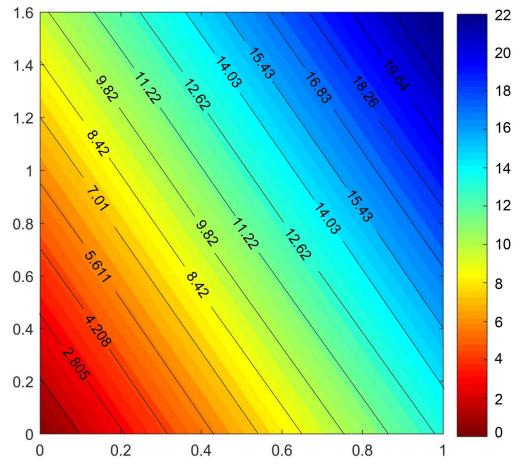it is vital to eliminate the effects of vegetation and surface roughness during the flood inundation process.

Figure 2. Absolute errors generated by different VOD and h parameter simulations.

We previously proposed a physics-based algorithm using SMAP TB to calibrate the attenuation of vegetation and surface roughness on the CYGNSS-derived SR [35]. The algorithm is based on the radiative transfer model to derive a combined parameter of the VOD (τ) and the surface roughness parameter (h), as $(-2\tau sec\theta - hcos\theta^2)$. The steps of the algorithm are summarized here.

Based on the bistatic radar equation, the SR considering the vegetation and surface roughness effects, hereafter named SR$_{cali}$, can be expressed as follows:

$$SR_{cali} = \frac{(4\pi)^2(R_{ts} + R_{sr})^2 P_r}{\lambda^2 P_t G_t G_r (exp(-2\tau sec\theta - hcos^2\theta))} \tag{1}$$

where P_r is the peak value of the analog delay waveform minus the DDM noise floor, R_{ts} is the distance from the transmitter to the SP, R_{sr} is the distance from the receiver to the SP, P_t is the peak power of the transmitted GPS signals, θ is the incident angle, G_t and G_r are the gains of the transmitter antenna and receiver antenna, respectively, τ is the VOD, and h is the surface roughness parameter [15].

Based on the radiative transfer model, the combined parameters of τ and h can be derived as follows:

$$exp\left(-2\tau sec\theta - hcos^2\theta\right) = \frac{T_{BV} - T_{BH}}{T_{BV}R_{H\_sm} - T_{BH}R_{V\_sm}} \tag{2}$$

where T_{BV} and T_{BH} are the H and V polarization SMAP TB, respectively, R_{H_sm} and R_{V_sm} are the effective reflectivity on the smooth dielectric boundary at H and V polarization, respectively, which are only related to the soil dielectric properties and the incidence angle, and can be estimated using Fresnel equations [36,37]. The incidence angle of the CYGNSS differs from the SMAP (i.e., 5–35° vs. 40°), thus leading to errors when substituting Equation (2) in Equation (1). The first-order Taylor expansion is then used to reduce the uncertainty from the incidence angle. For the details of the algorithm, please refer to [35].

3.2. Retrieval Algorithm

Carreno-Luengo et al., (2021) proposed a seasonal-threshold algorithm (STA) to detect the freeze/thaw state from CYGNSS data [14]. Here, an algorithm similar to the STA is proposed. The proposed flood inundation retrieval algorithm is based on the prevalence that the CYGNSS reflectivity is positively correlated with the wetting intensity of the land and a wetter surface will produce a stronger reflectivity [29]. It follows that different inundation levels can be distinguished using the SR_{cali}. The relationship between the inundation state and SR_{cali} can be represented by an index, where the high and low edges of inundation value represent the upper and bottom boundaries of the SR_{cali}, respectively. Based on analyzing the variation in the time series of the CYGNSS SR_{cali} and the relationship between the CYGNSS SR_{cali} and annual inundation states, we propose a new inundation detection index, namely the annual threshold flood inundation index (ATFII). For the SR_{cali} derived at time t, the annual scale ATFII is defined as follows:

$$ATFII = \frac{SR_{cali\_t} - SR_{cali\_min}}{SR_{cali\_max} - SR_{cali\_min}} \tag{3}$$

where SR_{cali_t} is the SR_{cali} derived at time t, and SR_{cali_min} and SR_{cali_max} are the maximum and minimum values of the SR_{cali} in one year, respectively. The ATFII index formula follows the structure and scaling of the normalized SR_{cali}.

For each CYGNSS point during the observation period, for each grid cell (9 × 9 km), grids with less than thirty observations are not used for calibration. The 5% largest numbers of one entire year are selected and the average value is calculated as the SR_{max} value, and vice versa for the SR_{min} value. The ATFII for each CYGNSS point is calculated from the number of points in the calibration period. This index can make full use of variations in the CYGNSS SR_{cali} and has the advantages of fast speed and convenience, which make it suitable for rapid inundation mapping.

Figure 3(a1,a2) are the average values of the maximum and minimum CYGNSS SR_{cali} during the seven-day average in 2021 in the southeast of China. Significant changes can be seen between the values of the maximum SR_{cali} (Figure 3(a1)) and minimum SR_{cali} (Figure 3(a2)). This variability is notably due to several extreme precipitations in 2021. Conversely, both reference values' standard deviation (SD) remains relatively stable, with the value over 60% of the areas below ~2 dB. The stable SD values contribute to the stability of the algorithm. After the ATFII retrieval, the next step is to discriminate the inundation state. Here, the floodwater fraction in the VIIRS is used as the benchmark, and the inundation data are derived from there. The VIIRS floodwater fraction is the percentage of open water in the VIIRS pixel, which represents the ratio of flooded land in the pixel. Here, the CYGNSS point is matched up with the VIIRS floodwater fraction data. As a result, the matched CYGNSS point has two values, i.e., the ATFII and floodwater fraction. The core concept of the classification is using the VIIRS floodwater fraction to identify the final threshold of the ATFII of different inundation grades. Considering the weight of the floodwater fraction, we divided the inundation grade into five categories. The grades are classified as "non-inundation", "mild-inundation", "moderate-inundation", "severe-inundation", and "inundated grid", for the floodwater fractions of 0, 0–20%, 20–50%, 50–80%, and >80%, respectively.
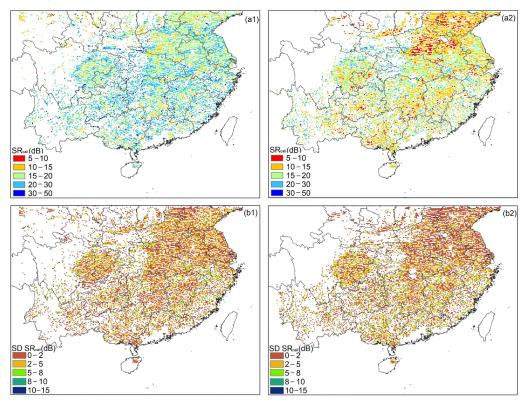
Figure 3. Averaged CYGNSS SR values in southeast China: (**a1**) the seven-day average of the maximum SR$_{cali}$ in July 2021, (**a2**) the seven-day average of the minimum SR$_{cali}$ during February 2021, (**b1**) the SD of the seven maximum values, and (**b2**) the SD of the seven minimum values.
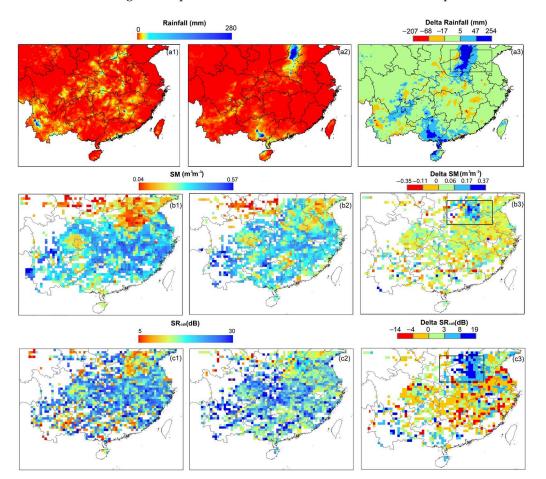
4. Results

4.1. Comparisons between the CYGNSS SR, SMAP SM, and GPM Precipitations

An evaluation of the sensitivity of the CYGNSS SR$_{cali}$ spatial pattern comparisons of the CYGNSS SR$_{cali}$, SMAP SM, and GPM precipitation on two different days, i.e., 17 July 2021 and 21 July 2021, in southeast China, is shown in Figure 4. The two days were chosen because extreme precipitation happened from 19 July 2021 to 22 July 2021. To show the continuous SR$_{cali}$ maps over southeast China, the CYGNSS SR$_{cali}$ and SMAP SM in Figure 4 are gridded to 36 km, which is not the optimal spatial resolution of this study.

Generally, the CYGNSS SR$_{cali}$ indicates good agreement with the SMAP SM. On 17 July 2021, the northern region of southeast China shows a lower SR$_{cali}$ value. However, on 21 July 2021, the value of the SR$_{cali}$ in the northern region tends to be significantly higher. In addition, the SR$_{cali}$ in the central area shows slight variation. This is consistent with the variations in the SMAP SM and GPM precipitation. The differences in the CYGNSS SR (Figure 4(c3)) are positive over the northeast, while negative over the middle of the region. The CYGNSS SR$_{cali}$ delta performs approximately the same as the differences in the GPM precipitation and SMAP SM shown in Figure 4(a3,b3), respectively.

4.2. VIIRS-ATFII Correlation in the Spatial and Temporal Distribution

Figure 5 shows the density plots of the CYGNSS ATFII with VIIRS floodwater fraction, and all correlation results are statistically significant with a significance level of 0.05 (*p*-value < 0.05). The color represents the point density. The data from one month of each season in 2021 were chosen to display the results. For each VIIRS pixel during the entire observation period, the CYGNSS observations located less than 187.5 from this pixel center were selected. To test the linearity of the CYGNSS-derived ATFII and VIIRS floodwater fraction correlation, the correlation coefficient (R) was used. However, it should be noted that a significant mismatch of the spatial scale exists between the VIIRS grid and the CYGNSS points (375 m vs. 3 × 0.5 km). Since data with different spatial resolutions

represent different feature characteristics, the differences in spatial resolution may result in biased data, leading to a dispersion between the VIIRS and the CYGNSS points.

Figure 4. Spatial patterns of the GPM precipitation, SMAP SM, and CYGNSS SR_{cali} in southeast China. (**a1–a3**) Precipitation on 17 July 2021 and 21 July 2021, and their differences (Delta GPM precipitation), (**b1–b3**) SMAP SM on 17 July 2021 and 21 July 2021, and their differences (Delta SM), and (**c1–c3**) CYGNSS SR_{cali} on 17 July 2021 and 21 July 2021, and their differences (Delta SR_{cali}).

To make a comprehensive assessment of the ATFII index and determine the values of different inundation grades, one-year CYGNSS ATFII data collected in 2020 were matched up with the ongoing VIIRS flood 375 m pixels. After matching them up with the VIIRS data, only high quality points were retained after filtering out low quality points with a 95% standard deviation. The ranges of the ATFII values for different inundation grades are shown in Table 1.

Table 1. Ranges of ATFII values for different inundation grades.

	Non-Inundation	Mild-Inundation	Moderate-Inundation	Severe-Inundation	Inundated Area
ATFII value	0–0.33	0.33–0.47	0.47–0.68	0.68–0.86	>0.86

Figure 6 shows the R values in southeast China for each month from January to December 2021. The average numbers of different inundation grades are also summarized. The mean percentages of the non-inundation grid statistics by the ATFII and VIIRS are 95.32% and 98.85%, respectively. To display the inundation grades in the range that intuitively makes sense, we do not show the numbers of non-inundation in Figure 6. The R value between the VIIRS flood product and ATFII varies from 0.51 to 0.64. It is particularly

noteworthy that, the R value shows a descending trend in the dry seasons, e.g., from January to May, similar to the result in Figure 5. As illustrated in Figure 6, the sample numbers vary from month to month and the proportion of the mild inundation grade is relatively low, with a ratio varying from 2.06% to 6.21%.
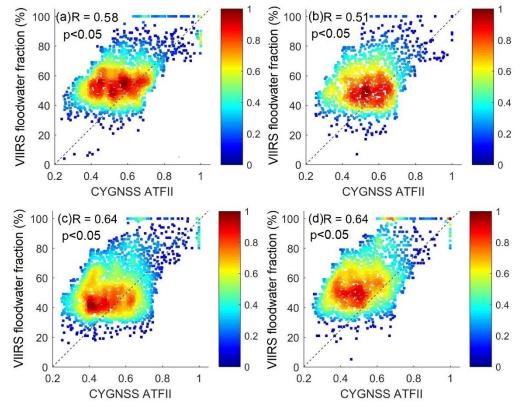

Figure 5. Comparison of the CYGNSS ATFII with VIIRS floodwater fraction in (**a**) January 2021, (**b**) April 2021, (**c**) July 2021, and (**d**) October 2021.
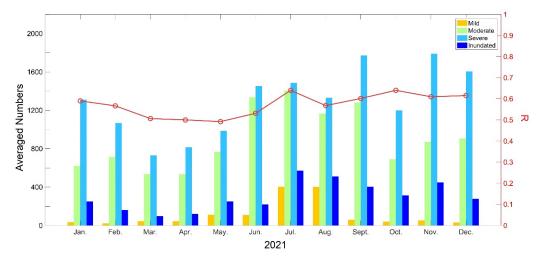

Figure 6. R values of the VIIRS floodwater fraction and CYGNSS-derived ATFII in 2021 in southeast China on a monthly basis.

Figure 7 shows the monthly probability density functions (PDFs) of the CYGNSS-derived ATFII and VIIRS from January to December 2021. Here, the grades of the VIIRS floodwater fractions are also divided into four categories: mild (water fraction is 0–20%), moderate (water fraction is 20–50%), severe (water fraction is 50–80%), and inundated area (water fractions >80%).
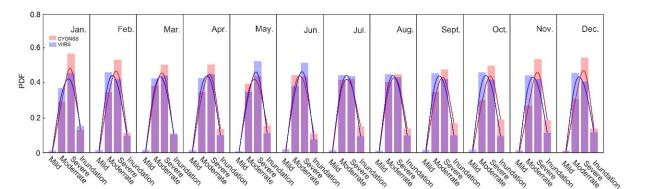
Figure 7. The PDFs of the inundation grades regarding the comparison between the VIIRS floodwater fraction and CYGNSS-derived ATFII monthly in 2021.

Generally, the inundation grades derived from ATFII well reflect the inundation dynamics during the observed period and indicate good agreement with the VIIRS. The CYGNSS-derived inundation grades vary significantly spatially. The PDFs from June to August outperform other months; in other words, the CYGNSS-derived inundation data have the best similarity distribution to the ATFII flood distribution data in this period. Meanwhile, the CYGNSS-derived inundation data have the lowest similarity to the ATFII flood distribution in January, November, and December. Note that the spatial differences between the two data can contribute to statistical error.

4.3. Variation Characteristics in CYGNSS-Derived Inundation Data during Extreme Precipitations

For an in-depth analysis of the performance of the CYGNSS-derived inundation grades, two extreme precipitation events happened in southeast China in 2021, i.e., from 17 to 23 July and from 19 to 25 August, with cumulative rainfalls exceeding 500 mm in some areas, selected as examples. Figure 8 shows the CYGNSS-derived inundation grades in southeast China before and after the two extreme precipitations. Obviously, the CYGNSS-derived inundation grades capture the high-intensity precipitation trends over the central and the eastern regions (shown by the red circles), respectively.

To demonstrate the CYGNSS-derived inundation grade characteristics, area ratio structure maps are shown in Figure 8(c1,c2), respectively. The severe and inundated areas in Figure 8(c1) improve from 14% to 22%, before and after the extreme precipitation, which occurred from 17 to 23 July 2021. Figure 8(c2) has a similar pattern to Figure 8(c1), with severe and inundated areas improving from 15% to 20%.

4.4. Validation of the CYGNSS Result with the SMAP SM and GPM Data

Figure 9 shows the results of the ATFII, SMAP SM, and precipitation variations during the observation period of two points in southeast China (lat: 34.24°, lon: 113.92°; lat: 39.12°, lon: 116.16°), respectively. The two points were chosen because of their high cumulative annual precipitation, both greater than 1000 mm. Three data types of time series were plotted: ATFII, SMAP SM ($m^3 m^{-3}$), and precipitation (mm).

As shown in Figure 9a, more than seven significant precipitation events (>40 mm) occurred, e.g., on day of year (DOY) 195, 200–202, 234, 244, and 267 during the observation period. Similar to Figure 9a, four significant precipitation events occurred, i.e., on DOY 183, 192, 210, 262, and 277–280, as illustrated in Figure 9b. Overall, the ATFII result demonstrates good agreement with precipitation and SMAP SM. Compared with Table 1, when the value of ATFII is greater than 0.47, the grid is regarded as moderately or severely inundated. The ATFII shows a high value during the significant precipitation events (box in Figure 9), which indicates that the area was flooded at this time. However, the ATFII is not always proportional to the precipitation (e.g., DOY 197–199 in Figure 9a, DOY 216–219 in Figure 9b). The poor quality of the CYGNSS data at this location may have led to this phenomenon.
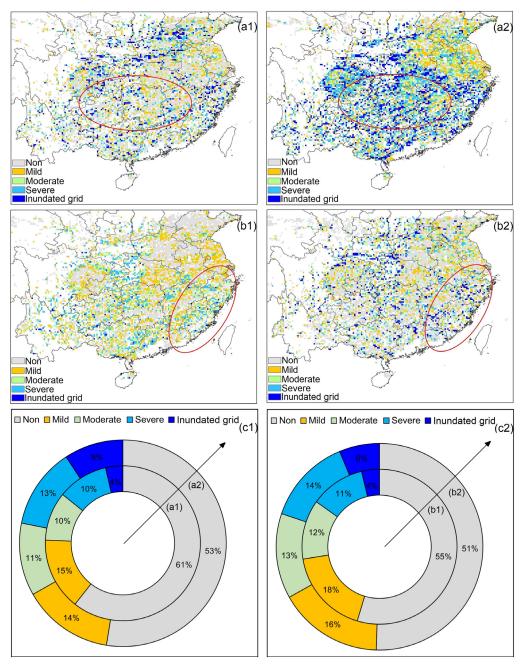
Figure 8. The CYGNSS-derived inundation grades in southeast China before and after two extreme precipitation events. (**a1**,**a2**) Inundation grade distributions before and after the extreme precipitations which occurred from 17 to 23 July 2021, respectively. (**b1**,**b2**) Inundation grade distributions before and after the precipitation which occurred from 19 to 25 August 2021, respectively. (**c1**,**c2**) The area ratios of (**a1**,**a2**,**b1**,**b2**), respectively.

It should be pointed out that, after DOY 310, the SMAP SM still has a slight increase. However, the ATFII and the precipitation do not change substantially. This indicates that the sensitivity of the ATFII to precipitation is higher than that of the SM. Moreover, the fluctuations in the ATFII are not as strong as the SM when precipitation is extremely high, e.g., when precipitation is greater than 100 mm. This may be because, in the ATFII retrieval algorithm, the maximum SR_{cali} is the mean value of 5% of the largest numbers, which may have had a slight smoothing effect on the extreme ATFII values, leading to a slight underestimation.
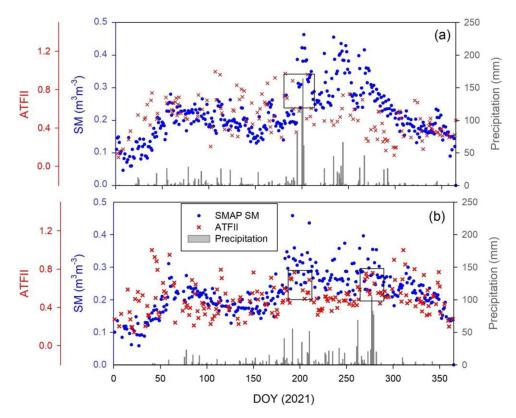
Figure 9. Variations in the ATFII, SMAP SM, and precipitation during the observation period of two points in the two study areas: (**a**) lat: 34.24°, lon: 113.92°, and (**b**) lat: 39.12°, lon: 116.16°.

4.5. A Case Study in Henan Province, China

The MODIS IGBP land cover map of the Henan Province is shown in Figure 10. Henan Province is located in central China (31.23°–36.22°N, 110.21°–116.39°E), and its topography is high in the west and low in the east. It consists mainly of plains and basins. The average annual rainfall in the region is 500–900 mm. We selected this area as a case because, in July 2021, a heavy precipitation disaster occurred in Henan due to the atmospheric circulation situation and the effect of the "Firework" typhoon in the western Pacific Ocean. On 19 July 2021, the cumulative surface average precipitation in Henan Province was 88 mm, of which the highest reached 361 mm. On 20–21 July 2021, heavy precipitation was mainly concentrated in Henan's western, northern, and central parts, with a cumulative precipitation of 627.4 mm. The maximum hourly precipitation on 20 July 2021 was 201.9 mm, which exceeded the historic extreme value for cumulative hourly precipitation in mainland China [29,30].

To provide consistency with the time series analysis, Figure 11 shows the CYGNSS-derived inundation grades in Henan Province from 19 July 2021 to 24 July 2021. Here, GPM precipitation data are also provided as a reference, to show the consistency in the CYGNSS-derived inundation grades and GPM precipitation. There are significant variations in CYGNSS-derived inundation grades from 20 July to 23 July due to the extreme precipitation event. By comparing the inundation results from Figure 11(a1–a6), the flood inundation is heavier in the northern and central areas, with mainly severe and full inundation grids. The area ratios of the severe and inundated grids are 0%, 19%, 52%, 56%, 25%, and 9%, respectively. In contrast, the inundation area is lighter in the southern regions, mainly the mild, moderate, or non-inundation soil, with similar spatial distribution characteristics from GPM precipitation. Note that in Figure 11(a4,a5), severe inundation events happened in the southern area; however, the GPM precipitation in Figure 11(b4,b5) is relatively small. The relatively severe inundation shown in Figure 11(a4,a5) may have been caused by the trapping of surface water due to persistent precipitation.
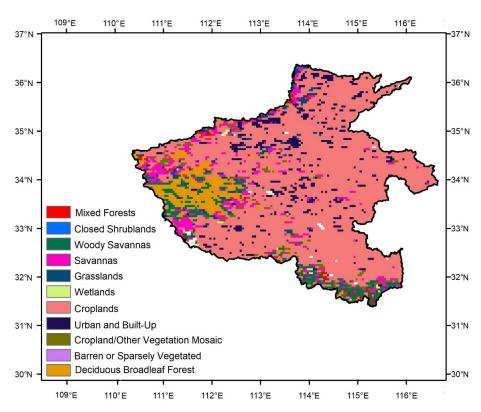
Figure 10. The MODIS IGBP land cover map of Henan Province.

Table 2 and Figure 12 show the fraction numbers and area ratios of inundation grades from Figure 11(a1,a6), respectively. From the perspective of continuous days, the area ratios of the grids with inundation are 54%, 53%, 98%, 98%, 84%, and 52%, respectively. Inundation was significantly higher on 21 July 2021 and 22 July 2021. In addition, the area ratios of precipitation greater than 100 mm from 20 July 2021 to 22 July 2021 were approximate 21%, 37%, and 11%, respectively. The inundation grade dynamics are associated with precipitation changes. Thus, CYGNSS-derived inundation grades perform well in estimating heavy precipitation.
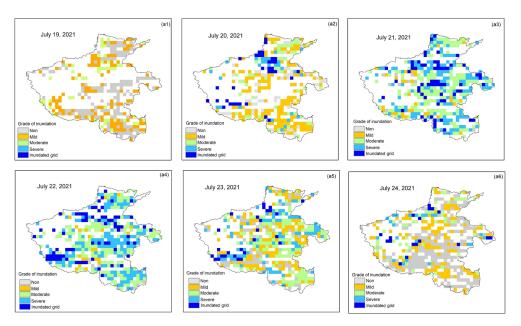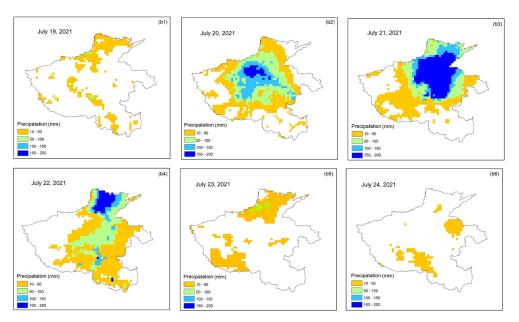

Figure 11. *Cont.*

Figure 11. The results of daily CYGNSS-derived inundation grades and GPM precipitation in Henan Province from 19 July 2021 to 24 July 2021. (**a1**–**a6**) CYGNSS-derived inundation grade distributions and (**b1**–**b6**) GPM precipitation distributions.
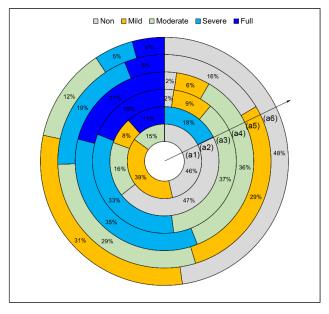

Figure 12. The area ratios of CYGNSS-derived inundation grades from 19 July 2021 to 24 July 2021. (**a1**–**a6**) represent the date from 19 July 2021 to 24 July 2021.

Table 2. The fractions of CYGNSS-derived inundation grades from 19 July 2021 to 24 July 2021.

Date	Non	Mild	Moderate	Severe	Full
19 July 2021	46%	39%	15%	0%	0%
20 July 2021	47%	8%	16%	18%	11%
21 July 2021	2%	9%	37%	33%	19%
22 July 2021	2%	6%	36%	35%	21%
23 July 2021	16%	29%	29%	19%	6%
24 July 2021	48%	31%	12%	5%	4%

5. Discussion

5.1. Influences of the Land Type

To evaluate land cover-related impacts on inundation retrieval, the R values between the VIIRS floodwater fraction and CYGNSS-derived ATFII were classified into twelve different land types derived from The International Geosphere-Biosphere Programme (IGBP), listed in Table 3. The R values perform well in evergreen needleleaf forest, mixed forest, woody savannas, grasslands, croplands, barren or sparsely vegetated, and cropland/natural vegetation mosaics, with R values greater than 0.55. Most of these areas represent relatively low vegetation cover, with the exception of the forest category. It can be concluded that vegetation cover can influence index calculation. Incoherent scattering caused by vegetation may contribute to this phenomenon. In contrast, the ATFII-VIIRS correspondence in urban and built-up areas performs worst, with R values smaller or equal to 0.5. The greater L band retrieval uncertainty in urban areas may lead to this phenomenon [3]. Note that some of the land types have only a few sample numbers for the statistics, e.g., evergreen needleleaf forest and barren or sparsely vegetated (number of points = 84 and 56, respectively), which may lead to a relatively large potential error.

Table 3. R values for twelve land types.

Land Type	Sample Numbers	R Value
Evergreen Needleleaf Forest	84	0.67
Evergreen Broadleaf Forest	956	0.58
Deciduous Broadleaf Forest	316	0.56
Mixed Forest	1040	0.59
Woody Savannas	3756	0.67
Savannas	11,839	0.52
Grasslands	3022	0.58
Permanent Wetlands	2390	0.50
Croplands	23,811	0.58
Urban and Built-up	3314	0.46
Cropland/Natural Vegetation Mosaic	3418	0.56
Barren or Sparsely Vegetated	56	0.57

5.2. Feasibility of Using CYGNSS to Detect Sub-Daily Flood Inundation Processes

This section evaluates the feasibility of the retrieved CYGNSS for sub-daily flood inundation retrieval. Since the CYGNSS has eight small satellites in orbit, it allows CYGNSS capability to perform sub-daily observations with a short revisit time. Figure 13 shows the CYGNSS-derived inundation grades in Henan Province, China, from 12 to 18 h and 18 to 24 h on 21 July 2020, respectively. Overall, Figure 13a captures the inundation spatial inundation pattern and provides the relatively detailed spatial variabilities in inundation. By contrast, the data in Figure 13b are sparsely distributed and cannot present as much detailed inundation information as in Figure 13a. Thus, it can be concluded that the CYGNSS can detect the sub-daily flood inundation processes in fine temporal resolution, but the performance of spatial distribution varies from hour to hour. Thus, one full day of the CYGNSS observation is used to evaluate flood inundation and provide the spatial distribution details.

5.3. Advantages and Limitations

In this study, we propose an index from CYGNSS data to retrieve flood inundation data and its grade on continuous observing days. The results show that the ATFII can retrieve flood inundation data with accuracy comparable to remote sensing flood products such as

the VIIRS. It can be concluded that our advantages exist in: (1) proposing an index model using CYGNSS data, which has superior abilities to retrieve flood inundation information in more detail and at rapid timescales, and with the advantages of fast speed and convenience; (2) classifying inundation states into different grades based on the ATFII values, which provides a new way of deriving inundation grade variations, where the CYGNSS-derived inundation grades show stable and robust abilities for identifying inundation states in different months; and (3) the higher temporal sampling of the CYGNSS compared to more traditional remote sensing techniques, e.g., passive remote sensing, which can open new insights into monitoring highly dynamic inundation processes.
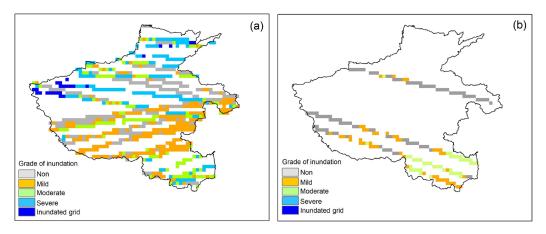

Figure 13. The results of sub-daily CYGNSS-derived inundation grades in Henan Province on 21 July 2020. (**a**) CYGNSS-derived inundation grades from 12 to 18 h and (**b**) CYGNSS-derived inundation grades from 18 to 24 h.

However, there are still some limitations in this study. First, the inundation grade threshold accuracy depends on the VIIRS flood data. As mentioned above, a spatial scale mismatch exists between the VIIRS grid and the CYGNSS points. Although the point-to-pixel matching method is used to reduce this well-known issue, different spatial scales between the CYGNSS and VIIRS may lead to significant errors. Another limitation is that no-data grids still exist in the daily flood inundation results. Since the CYGNSS data are distributed discretely, a simple interpolation may lead to significant discontinuities in the results and low accuracy. In the future, the algorithm for filling the daily no-data grids will be a critical issue. The ATFII combined with other flood inundation datasets, e.g., MODIS and Landsat, is worth consideration.

6. Conclusions

Mapping the distribution of flood inundation is of great importance to understanding its environmental impacts. In contrast to the state-of-the-art methods focusing on investigating the feasibility of using CYGNSS signals to obtain flood inundation, this study proposes an index named ATFII to monitor flood inundation from CYGNSS measurements, and the grades of flood inundation were quantified. The resulting ATFII shows consistent spatial patterns with the VIIRS flood product and GPM precipitation data. The main conclusions include, but are not limited to, the following aspects:

(1) For monthly results, the R value between the VIIRS flood product and ATFII varies from 0.51 to 0.64, with an acceptable significance level ($p < 0.05$);

(2) The ATFII is qualitatively consistent with the VIIRS flood product, GPM-derived precipitation, and SMAP SM. It provides a spatiotemporal distribution of flood inundation with high accuracy;

(3) The CYNSS-derived ATFII can strengthen knowledge and be complementary to the existing flood products. For example, the CYNSS-derived ATFII can provide helpful

information on a large scale with vegetation calibration, when the current flood products have challenges in identifying water under vegetation;

(4) The inundation grade variations classified by the ATFII can capture the spatial variation in inundation. The results could support the timely retrieval of flood inundation data and changes in its extent.

Considering these findings, the good quality of the flood inundation results from the CYGNSS could help in studying the behavior of inundation in response to the projection of environmental impacts. In addition, since the currently launched spaceborne GNSS-R missions are very similar in terms of detection mechanisms and data recording modes, the index is expected to have broad applications for other current and upcoming spaceborne GNSS-R missions.

Author Contributions: Conceptualization, T.Y., Z.S. and L.J.; methodology, T.Y.; validation, T.Y.; formal analysis T.Y.; resources, L.J.; writing—original draft preparation, T.Y.; writing—review and editing, T.Y. and Z.S.; supervision, Z.S. and L.J.; funding acquisition, T.Y. and Z.S. All authors have read and agreed to the published version of the manuscript.

Data Availability Statement: Not applicable.

Conflicts of Interest: The authors declare no conflict of interest.

References

1. Schumann, G.; Bates, P.D.; Horritt, M.S.; Matgen, P.; Pappenberger, F. Progress in integration of remote sensing–derived flood extent and stage data and hydraulic models. *Rev. Geophy.* **2009**, *47*, RG4001. [CrossRef]
2. Chew, C.; Reager, J.T.; Small, E. CYGNSS data map flood inundation during the 2017 Atlantic hurricane season. *Sci. Rep.* **2018**, *8*, 9336. [CrossRef] [PubMed]
3. Wu, H.; Kimball, J.S.; Zhou, N.; Alfieri, L.; Luo, L.; Du, J.; Huang, Z. Evaluation of real-time global flood modeling with satellite surface inundation observations from SMAP. *Remote Sens. Environ.* **2019**, *233*, 111360. [CrossRef]
4. Gudmundsson, L.; Boulange, J.; Do, H.X.; Gosling, S.N.; Zhao, F. Globally observed trends in mean and extreme river flow attributed to climate change. *Science* **2021**, *371*, 1159–1162. [CrossRef]
5. Yin, J.; Guo, S.; Gentine, P.; Sullivan, S.C.; Liu, P. Does the hook structure constrain future flood intensification under anthropogenic climate warming? *Water. Resour. Res.* **2021**, *57*, e2020WR028491. [CrossRef]
6. Apel, H.; Thieken, A.H.; Merz, B.; Blöschl, G. Flood risk assessment and associated uncertainty. *Nat. Hazards Earth Syst. Sci.* **2004**, *4*, 295–308. [CrossRef]
7. Sanyal, J.; Lu, X. Application of remote sensing in flood management with special reference to monsoon asia: A review. *Nat. Hazards J. Int. Soc. Prev. Mitig. Nat. Hazards* **2004**, *33*, 283–301. [CrossRef]
8. Tegos, A.; Ziogas, A.; Bellos, V.; Tzimas, A. Forensic Hydrology: A Complete Reconstruction of an Extreme Flood Event in Data-Scarce Area. *Hydrology* **2022**, *9*, 93. [CrossRef]
9. Rahman, M.S.; Di, L. The state of the art of spaceborne remote sensing in flood management. *Nat. Hazards* **2017**, *85*, 1223–1248. [CrossRef]
10. McCormack, T.; Campanyà, J.; Naughton, O. A methodology for mapping annual flood extent using multi-temporal Sentinel-1 imagery. *Remote Sens. Environ.* **2022**, *282*, 113273. [CrossRef]
11. Zhao, J.; Pelich, R.; Hostache, R.; Matgen, P.; Wagner, W.; Chini, M. A large-scale 2005–2012 flood map record derived from ENVISAT-ASAR data: United Kingdom as a test case. *Remote Sens. Environ.* **2021**, *256*, 112338. [CrossRef]
12. DeVries, B.; Huang, C.; Armston, J.; Huang, W.; Jones, J.W.; Lang, M.W. Rapid and robust monitoring of flood events using Sentinel-1 and Landsat data on the Google Earth Engine. *Remote Sens. Environ.* **2020**, *240*, 111664. [CrossRef]
13. Li, S.; Goldberg, M.; Kalluri, S.; Lindsey, D.T.; Sjoberg, B.; Zhou, L.; Helfrich, S.; Green, D.; Borges, D.; Yang, T.; et al. High Resolution 3D Mapping of Hurricane Flooding from Moderate-Resolution Operational Satellites. *Remote Sens.* **2022**, *14*, 5445. [CrossRef]
14. Carreno-Luengo, H.; Ruf, C.S. Retrieving Freeze/Thaw Surface State From CYGNSS Measurements. *IEEE Trans. Geosci. Remote Sens.* **2022**, *60*, 4302313. [CrossRef]
15. Chew, C.; Small, E. Soil Moisture Sensing Using Spaceborne GNSS Reflections: Comparison of CYGNSS Reflectivity to SMAP Soil Moisture. *Geophys. Res. Lett.* **2018**, *45*, 4049–4057. [CrossRef]

16. Ruf, C.S.; Chang, P.S.; Clarizia, M.P.; Gleason, S.; Jelenak, Z.; Murray, J.; Morris, M.; Musko, S.; Posselt, D.; Provost, D.; et al. CYGNSS Handbook. Available online: https://cygnss.engin.umich.edu/wp-content/uploads/sites/534/2021/06/CYGNSS_Handbook_April2016.pdf (accessed on 1 April 2016).

17. Ruf, C.S.; Chew, C.; Lang, T.; Morris, M.G.; Nave, K.; Ridley, A.; Balasubramaniam, R. A New Paradigm in Earth Environmental Monitoring with the CYGNSS Small Satellite Constellation. *Sci. Rep.* **2018**, *8*, 8782. [CrossRef] [PubMed]

18. Loria, E.; O'Brien, A.; Zavorotny, V.; Downs, B.; Zuffada, C. Analysis of scattering characteristics from inland bodies of water observed by CYGNSS. *Remote Sens. Environ.* **2020**, *245*, 111825. [CrossRef]

19. Mayers, D.; Ruf, C. Measuring Ice Thickness with Cygnss Altimetry. In Proceedings of the IGARSS 2018—2018 IEEE International Geoscience and Remote Sensing Symposium, Valencia, Spain, 22–27 July 2018; pp. 8535–8538.

20. Li, W.; Cardellach, E.; Fabra, F.; Ribó, S.; Rius, A. Assessment of Spaceborne GNSS-R Ocean Altimetry Performance Using CYGNSS Mission Raw Data. *IEEE Trans. Geosci. Remote Sens.* **2019**, *58*, 238–250. [CrossRef]

21. Ruf, C.S.; Gleason, S.; McKague, D.S. Assessment of CYGNSS Wind Speed Retrieval Uncertainty. *IEEE J. Sel. Top. Appl. Earth Obs. Remote Sens.* **2019**, *12*, 87–97. [CrossRef]

22. Clarizia, M.P.; Ruf, C.S. Wind Speed Retrieval Algorithm for the Cyclone Global Navigation Satellite System (CYGNSS) Mission. *IEEE Trans. Geosci. Remote Sens.* **2016**, *54*, 4419–4432. [CrossRef]

23. Liu, B.; Wan, W.; Guo, Z.; Ji, R.; Wang, T.; Tang, G.; Cui, Y.; Hong, Y. First Assessment of CyGNSS-Incorporated SMAP Sea Surface Salinity Retrieval Over Pan-Tropical Ocean. *IEEE J. Sel. Top. Appl. Earth Obs. Remote Sens.* **2021**, *14*, 12163–12173. [CrossRef]

24. Morris, M.; Chew, C.; Reager, J.T.; Shah, R.; Zuffada, C. A novel approach to monitoring wetland dynamics using CYGNSS: Everglades case study. *Remote Sens. Environ.* **2019**, *233*, 111417. [CrossRef]

25. Gerlein-Safdi, C.; Ruf, C.S. A CYGNSS-Based Algorithm for the Detection of Inland Waterbodies. *Geophys. Res. Lett.* **2019**, *46*, 12065–12072. [CrossRef]

26. Wan, W.; Liu, B.; Zeng, Z.; Chen, X.; Wu, G.; Xu, L.; Chen, X.; Hong, Y. Using CYGNSS Data to Monitor China's Flood Inundation during Typhoon and Extreme Precipitation Events in 2017. *Remote Sens.* **2019**, *11*, 854. [CrossRef]

27. Chew, C.; Small, E. Estimating inundation extent using CYGNSS data: A conceptual modeling study. *Remote Sens. Environ.* **2022**, *246*, 111869. [CrossRef]

28. Unnithan, S.L.K.; Biswal, B.; Rüdiger, C. Flood Inundation Mapping by Combining GNSS-R Signals with Topographical Information. *Remote Sens.* **2020**, *12*, 3026. [CrossRef]

29. Zhang, S.; Ma, Z.; Li, Z.; Zhang, P.; Liu, Q.; Nan, Y.; Zhang, J.; Hu, S.; Feng, Y.; Zhao, H. Using CYGNSS Data to Map Flood Inundation during the 2021 Extreme Precipitation in Henan Province, China. *Remote Sens.* **2021**, *13*, 5181. [CrossRef]

30. Yang, W.; Gao, F.; Xu, T.; Wang, N.; Tu, J.; Jing, L.; Kong, Y. Daily Flood Monitoring Based on Spaceborne GNSS-R Data: A Case Study on Henan, China. *Remote Sens.* **2021**, *13*, 4561. [CrossRef]

31. Gleason, S.; Ruf, C.S.; O'Brien, A.J.; McKague, D.S. The CYGNSS Level 1 Calibration Algorithm and Error Analysis Based on On-Orbit Measurements. *IEEE J. Sel. Top. Appl. Earth Obs. Remote Sens.* **2019**, *12*, 37–49. [CrossRef]

32. Eroglu, O.; Kurum, M.; Boyd, D.; Gurbuz, A.C. High Spatio-Temporal Resolution CYGNSS Soil Moisture Estimates Using Artificial Neural Networks. *Remote Sens.* **2019**, *11*, 2272. [CrossRef]

33. Li, S.; Sun, D.; Goldberg, M.D.; Sjoberg, B.; Santek, D.; Hoffman, J.P.; DeWeese, M.; Restrepo, P.; Lindsey, S.; Holloway, E. Automatic near real-time flood detection using Suomi-NPP/VIIRS data. *Remote Sens. Environ.* **2018**, *204*, 672–689. [CrossRef]

34. Skofronick-Jackson, G.; Petersen, W.A.; Berg, W.; Kidd, C.; Stocker, E.F.; Kirschbaum, D.B.; Kakar, R.; Braun, S.A.; Huffman, G.J.; Iguchi, T.; et al. The Global Precipitation Measurement (GPM) Mission for Science and Society. *BAMS* **2017**, *98*, 1679–1695. [CrossRef] [PubMed]

35. Yang, T.; Wan, W.; Wang, J.; Liu, B.; Sun, Z. A Physics-Based Algorithm to Couple CYGNSS Surface Reflectivity and SMAP Brightness Temperature Estimates for Accurate Soil Moisture Retrieval. *IEEE Trans. Geosci. Remote Sens.* **2022**, *60*, 4409715. [CrossRef]

36. Choudhury, B.J.; Schmugge, T.J.; Chang, A.; Newton, R.W. Effect of surface roughness on the microwave emission from soils. *J. Geophys. Res.* **1979**, *84*, 5699–5706. [CrossRef]

37. Panciera, R.; Walker, J.P.; Jackson, T.J.; Gray, D.A.; Tanase, M.A.; Ryu, D.; Monerris, A.; Yardley, H.; Rüdiger, C.; Wu, X.; et al. The soil moisture active passive experiments (SMAPEx): Toward soil moisture retrieval from the SMAP mission. *IEEE Trans. Geosci. Remote Sens.* **2013**, *52*, 490–507. [CrossRef]